Multi-dimensional Smouldering Model: Concepts, Validation, and Applications

Seyed Ziaedin Miry [a*], Marco A.B. Zanoni [a], Tarek L. Rashwan [a,b], Jason I. Gerhard [a]

[a] Department of Civil and Environmental Engineering, The University of Western Ontario, London, Ontario N6A 5B9, Canada

[b] Department of Civil Engineering, Lassonde School of Engineering, York University, Toronto, Ontario, M3J 1P3, Canada [1]

[1] Current address

Abstract:

Applied smouldering systems are gaining popularity for a variety of energy conversion applications. Radial heat loss plays a crucial role in these systems, as they cause multi-dimensional effects (e.g., in temperature, airflow, and chemical activity). These effects can control system operation limits and performance; therefore, a robust understanding of these multi-dimensional effects is crucial for design engineers. A multi-dimensional applied smouldering numerical model was developed that couples key physics and chemistry. The model was validated against highly instrumented, multi-dimensional smouldering experiments. The model was then employed to obtain a qualitative investigation of multi-dimensional effects and quantitative analysis of the energy balance that dictates the limits of the self-sustaining process. Moreover, a sensitivity analysis of the system energy efficiency was completed. The results provide insight into the interconnected nature of key physical (e.g., temperature, air flow, porous beds) and chemical (e.g., oxygen concentration, reaction intensity) qualities. Altogether, this work provides a novel tool for investigating, designing, and optimizing smouldering reactors for a range of applications such as soil remediation, waste-to-energy, and improving sanitation in the developing world.

[*] Corresponding author at: Department of Civil and Environmental Engineering, The University of Western Ontario, Claudette Mackay-Lassonde Pavilion, Rm. 1317, London, Ontario, Canada N6A 5B9. E-mail address: smiry@uwo.ca (S.Z. Miry)

Keywords:

Thermal treatment
Smouldering combustion
Porous medium
Heat losses
Multi-dimensional numerical modelling
Model validation

Nomenclature

Latin Letters	
A_{GAC}	Pre-exponential factor, s^{-1}
A_s	Surface area per unit volume of the porous medium, m^2
C	Fuel concentration
C_p	Specific heat capacity, J kg^{-1} K^{-1}
d_p	Particle diameter, m
D_g	Diffusion coefficient, m^2 s^{-1}
E_{GAC}	Activation energy, kJ mol^{-1}
H	Radial heat transfer coefficient, W m^{-2} K^{-1}
h_{sg}	Interstitial heat transfer coefficient, W m^{-2} K^{-1}
k	Thermal conductivity, W m^{-1} K^{-1}
k_p	Intrinsic permeability, m^2
L	Column length, m
M_g	Molar weight, g mol^{-1}
m	Total Mass, kg
Nu	Nusselt number
P	Pressure, Pa
Pr	Prandtl number
$\dot{q}$	Heat flux, W m^{-2}
R	Column radius, m
R_{GAC}	Reaction rate, s^{-1}
Re	Reynolds number
R_g	Ideal gas constant, J mol^{-1} K^{-1}
T	Temperature, °C
u	Darcy air flux, m s^{-1}
ν_f	Smouldering front velocity, cm min^{-1}
ν_{O_2}	Oxygen stoichiometric coefficient, kg.O_2 kg.$fuel^{-1}$
Y	Mass fraction
Greek Symbols	
ΔH	Heat of oxidation, MJ kg^{-1}

μ	Dynamic viscosity, Pa s
ρ	Density, kg m^{-3}
ϕ	Porosity
σ	Stefan-Boltzmann constant, W m^{-2} K^{-4}
Subscripts/Superscripts	
b	Bulk
eff	Effective
g	Gas
GAC	Granular Activated Carbon
i	Metal Sheet
in	Inlet
p	Peak
r	Radial Direction
rad	Radiation
s	Solid
sp	Spherical
z	Vertical Direction
0	Initial value
rad	Radiation
sp	Sphere

1. Introduction

Thermal porous medium reactors are used for a variety of applications, including: (*i*) phase change materials (PCM) [1], (*ii*) sensible [2] and thermochemical energy storage [3], (*iii*) waste-to-energy and resource recovery [4, 5], (*iv*) pyrolysis and gasification (e.g., for CO and H_2 production) [6-8], (*v*) household and food industry (e.g., hot water production) [9, 10], and (*vi*) applied smouldering of organic liquids/solids (e.g., faeces [11], wastewater sludge [12], granular activated carbon [13, 14], coal tar [15], bitumen [16]) embedded in an inert porous matrix (e.g., sand, soil). Applied smouldering has been successfully implemented in different reactors from laboratory scale (e.g., column, 0.003 m^3) to intermediate (e.g., Drum, 0.3 m^3) and pilot field-scale (e.g., bin or Hottpad, 3 m^3) [17-20].

Applied smouldering systems are typically operated as a "self-sustaining" process, meaning that the reaction will propagate, after a local and short ignition event, without further external energy. Self-sustained smouldering results from a local, positive energy balance (i.e., energy released from smouldering exceeds all losses locally at the reaction front). Self-sustaining makes applied smouldering an energy efficient, cost effective, and green technology [21]. When the energy balance becomes negative (e.g., due to high heat losses [16]), the reaction can weaken towards extinction [22]. Radial heat losses from the hot inert porous bed trailing smouldering is responsible for transferring 28-52% of total energy generated out of the system in lab scale experiments [16, 23]. Moreover, heat losses cause a non-uniform temperature and air flow distribution (i.e., non-uniform air flux) along the radius of the reactor [23-26]. These factors can decrease the smouldering robustness (i.e., resistance of self-sustaining reaction to extinction) from center to the wall (i.e., non-uniform reactions [27]). These multi-dimensional effects can deteriorate the system performance and lead to unexpected failures; however, the interplay between these effects is not well-understood [28].

The effects of radial heat losses in smouldering reactors were analyzed via analytical modelling [29]. A System Energy Efficiency (SEE) analysis was developed using a global energy balance to investigate the system sensitivity to reactor radius (R) and quality of the surrounding insulation (represented by a heat loss coefficient, H) [29]. That study quantified the diminishing influence of radial heat losses with increasing reactor radius (e.g., 35% of the energy was lost radially in a batch reactor with R = 8 cm compared to 14% with R = 30 cm [29]). These results align with experimental studies that show increasing scale led to reduced heat losses and extended thresholds for self-sustained smouldering [30, 31] and smouldering robustness.

Smouldering includes heat and mass transfer processes in porous media coupled with chemical reactions. Figure 1 shows self-sustaining smouldering reactions, which propagate through the bed in the direction of air flow, and composed of multiple distinct zones including (i) preheating, (ii) reaction, and (iii) cooling. Each exhibits dominant physical and chemical processes [32, 33]. The key processes happening in each zone are summarized in [33] and also in the methodology section. By propagating the self-sustained smouldering in the system, these three interdependent zones extend in thickness and intensity throughout space and time.

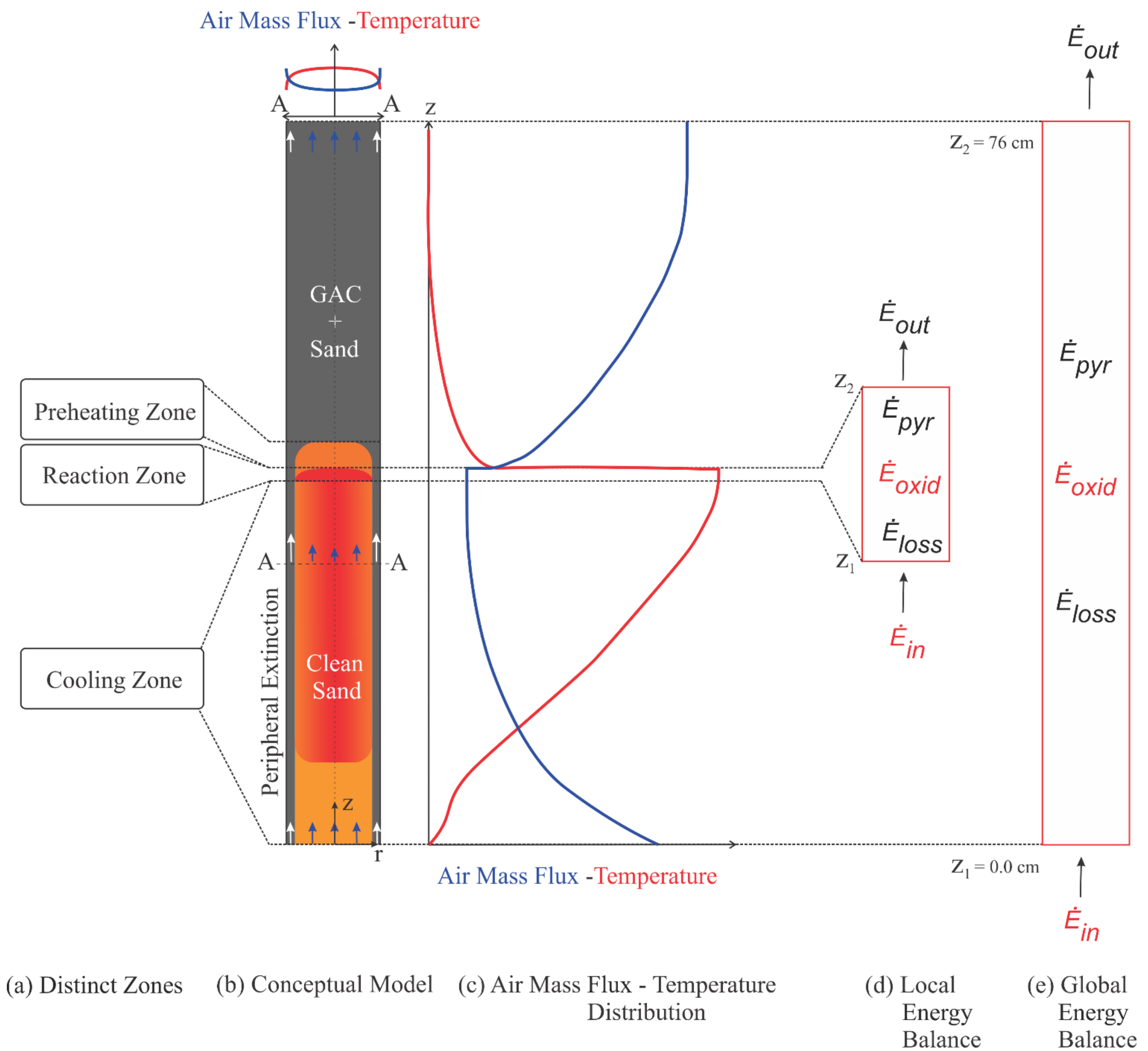

Figure 1. (a) Multiple distinct zones of applied smoldering reactor. (b) Conceptual model showing a distorted smouldering front (red) that propagate through the contaminated region (gray) and leaving clean and hot sand (orange) behind while radial heat loss causes peripheral extinction. (c) Air mass flux and temperature distribution at a specific time. (d) Local and (e) global energy balance analysis.

One-dimensional (1D) smouldering models were used to investigate the effect of chemical mechanisms [34-36] and extinction criteria [16, 22, 37]. In such models, a global heat loss coefficient is employed as a sink term [16, 22, 33], and it is usually adjusted to match the slope of the experimental centreline temperature behaviour [24]. The fraction of carbon oxidized and the fraction of oxygen consumed depend on the front temperature, which is affected by heat losses [26]. While these 1D models elucidate useful features, they cannot capture key multi-dimensional effects, e.g., smouldering front distortions [23, 26], non-uniform air flux [23, 38]. These important features have been suggested by analytical calculations [38] and experiments [25, 26, 28] to drive peripheral extinction (i.e., unconsumed fuel near the wall) due to radial heat losses [25, 27]; see Fig. 1. Previous 2D smouldering numerical modelling are summarized in Table 1.

Table 1. 2D numerical smouldering models available in the literature

Porous Medium	**Fuel**	**Motivation**	**Discussion**	**Ref**
Alumina Bead	Carbon	- Heat loss - Front shape stability	- Effect of radial heat loss - Smouldering front shape	[23]
Peat	Peat	- Heat loss - Shrinkage of structure	- Effect of radial heat loss and inorganic content - Structure of natural downward smouldering	[27]
Cellulosic material	Cellulosic material	- Heat loss	- Investigation of the mechanisms controlling smouldering	[39]
Polyurethane foam	Polyurethane foam	- Heat loss	- Investigation of the complexity of the reaction mechanism - Effect of radial heat loss	[40]
Charcoal	Charcoal	- Heat loss	- Investigation of oxygen concentration	[41]
Foam insulation	Foam insulation	- Heat loss	- Effect of radial heat loss	[42]
Foam insulation	Foam insulation	- Heat loss	- Effect of radial heat loss	[43]
Carbonaceous rod	Carbonaceous rod	- Heat loss - Diffusion of oxygen	- Effect of radial heat loss and oxygen distribution	[44]
Cigarette	Cigarette	- Heat loss - Diffusion of oxygen	- Effect of radial heat loss - Radial oxygen mass transfer	[45]
Porous object	Porous object	- Heat loss	- Air flow distribution	[38]
Sand/soil/	Waste oil sludge (WOS)	- Bed heterogeneity (e.g., WOS concentration, sand/soil permeability)	- Proof of concept, sensitivity analysis, and design of Hottpad	[20]
Soil	Coal tar	- Heterogeneity	- Effect of Coal tar and permeability heterogeneity	[46]
Sand	Coal tar	- Multi-dimension-al air flow field	- Smouldering propagation - Thermal robustness	[47]

The studies in Table 2 generally developed and validated 2D numerical models to show the effects of radial heat losses on the non-uniformity of temperature [27, 44, 45], air flux [23, 38], oxygen mass fraction [41, 43] and chemistry distribution that affect the smouldering front shape, velocity, and propagation [23, 27, 44].

Previous 2D studies showed peripheral extinction [27, 39, 40] with the centerline self-sustaining smouldering weakening to global quenching (i.e., complete extinction) by increasing radial heat losses (e.g., $H > 20$ W/m^2 K). Heat losses also lowered temperatures [45] and oxygen consumption near the wall in comparison to the centerline [43]. Increasing the radial heat loss decreased the smouldering front velocity because of decreasing temperature and reaction rate (i.e., char mass fraction distribution) [39, 42] and, by increasing the radial heat transfer coefficient from 20 to 100 W/m^2 K, the maximum temperature and smouldering front velocity decreased to roughly one third [44]. Pozzobon et al. [23] performed a numerical and experimental investigation of radial heat loss effect in temperature distribution, smouldering front shape, and oxygen consumption. They showed that, by decreasing the fuel mass concentration from 3.6 to 2.3%, the smouldering front shape was inverted from concave to convex. This shift in the smouldering front shape was hypothesized to result from a competition between non-uniform reactions and non-uniform air flux; but this hypothesis has not yet been rigorously tested.

A phenomenological 2D numerical model capable of simulating smouldering in heterogeneous domains was developed to simulate applied smouldering [20, 46, 47]. This model was validated to perform sensitivity analyses on key design parameters of commercial-scale systems, including permeability heterogeneity in and fuel concentration (here, waste oil sludge (WOS) saturation). Valuable practical insight was achieved through this modelling. For example, it was shown that smouldering systems could operate well with high levels of heterogeneity in WOS saturation (e.g., due to poor-mixing), but were highly sensitive to heterogeneity in the soil permeability (e.g., from using a widely graded soil). However, that model was not capable of simulating coupled effects with heat losses (e.g., non-uniform reactions and non-uniform air flux).

Considering the previous research, it is not entirely clear how coupled non-uniformities (e.g., in temperature, air flux, and reactions) will affect applied smouldering under a range of conditions relevant for applications. Therefore, this study aims to address this knowledge gap by combining the most rigorous components of established smouldering models into a new, multi-dimensional numerical model. Towards this goal, this study aimed to: (*i*) develop a 2D numerical model to simulate 2D heat transfer in an inert porous medium; (*ii*) conduct heating experiments, i.e., no fuel within the porous medium, to validate the heat transfer model; (*iii*) develop a simple chemical mechanism for granular activated carbon (GAC) smouldering; (*iv*) develop a 2D smouldering model applying the developed chemical mechanism; (*v*) conduct 2D GAC smouldering experiments to validate the smouldering model; (*vi*) use the validated model to resolve the global energy balance dynamics, (*vii*) perform qualitative and quantitative analysis of the factors that promote global and local smouldering quenching. Altogether, this work provides novel insights into the global energy balance and multi-dimensional effects in applied smouldering systems, which are also beneficial for other thermal porous media technologies.

2. Methodology

2.1 Modelling

An axisymmetric, 2D numerical model was developed in COMSOL Multiphysics (Version 5.5) using high resolution of 0.05 cm discretization. The computational domain used cylindrical coordinates and simulated: (*i*) a porous medium composed of clean sand mixed with granular activated carbon (GAC) and (*ii*) a surrounding, solid metal sheet representing the column stainless steel wall. The model dimensions mirrored the experimental setup in Fig. 2. The governing equations (Eqs. (1-17)) were solved at every node in space and time to simulate 2D smouldering and heat transfer. The numerical model considered two phases: (*i*) solid (i.e., GAC, sand) and (*ii*) gas. Pyrolysis reactions were assumed to be negligible [30, 48, 49], as the GAC used was nearly entirely carbon (> 90%) and exhibited low volatiles content [13, 30]. Moreover, thermogravimetric experiments performed on GAC under an inert atmosphere (i.e., using nitrogen) resulted in a negligible mass loss (Supplementary Material, Section C). Therefore, the GAC smouldering kinetics followed a global, 1-step oxidation mechanism [13]:

$$GAC + \nu_{O_2} O_2 \xrightarrow{R_{GAC}} \nu_{co}\, CO + \nu_{co_2}\, CO_2 \tag{1}$$

where the oxidation reaction rate (R_{GAC}) was described as a first-order Arrhenius reaction [50] :

$$R_{GAC} = A_{GAC} exp\left(-\frac{E_{GAC}}{R_g T_s}\right)(Y_{GAC})(Y_{O_2}) \tag{2}$$

where A_{GAC} is the pre-exponential factor, E_{GAC} is the activation energy, T_s is the solid temperature, and ν_{O_2} is the oxygen stoichiometric coefficient. The mass fraction of GAC and oxygen are defined as $Y_{GAC} = m_{GAC}/m_{GAC,0}$ and $Y_{O_2} = m_{O_2}/m_{air}$, the subscript "*0*" refers to *initial*, and m_{GAC} and m_{O_2} are the mass of GAC and oxygen, respectively. The kinetic parameters (A and E) were estimated via a Genetic Algorithm (GA) optimization method coupled with thermogravimetric experiments performed under an oxidative atmosphere (i.e., using air; see Supplementary Material, Section C). Although the use of the Arrhenius equation and reaction rates for heterogeneous reactions has been questioned [51-54], this simplistic approach is extensively used in the literature of thermal degradation of solids and liquids [13, 32, 36, 55]. While it is beyond the scope of this paper, it is worth noting that the rate of a heterogeneous reaction should explicitly consider the decrease in reactant-product surface area as the reaction consumes the solid surface [51-54]. This dependency is approximated in Eq. (2) via including Y_{GAC}.

The conservation of mass for the solid phase is [13]:

$$\frac{\partial(Y_{GAC})}{\partial t} = -R_{GAC} \tag{3}$$

and the gas phase is [23, 43]:

$$\frac{\partial(\rho_g\phi_g)}{\partial t} + \frac{1}{r}\frac{\partial(r\rho_g u_r)}{\partial r} + \frac{\partial(\rho_g u_z)}{\partial z} = Q_g \tag{4}$$

where Q_g represents the volumetric mass generation rate for the gas phase:

$$Q_g = (\varphi_{GAC}\rho_{GAC})(R_{GAC}) \tag{5}$$

The bulk transport of oxygen in the gas phase was described by Eq. (6) [13]:

$$\phi_g\frac{\partial(\rho_g Y_{O_2})}{\partial t} + \frac{\partial(\rho_g u_r Y_{O_2})}{\partial r} + \frac{\partial(\rho_g u_z Y_{O_2})}{\partial z} = \frac{1}{r}\frac{\partial}{\partial r}\left(r\phi_g\rho_g D_g\frac{\partial Y_{O_2}}{\partial r}\right) + \frac{\partial}{\partial z}\left(\phi_g\rho_g D_g\frac{\partial Y_{O_2}}{\partial z}\right) + Q_{O_2} \tag{6}$$

where D_g is the diffusion coefficient, Y_{O_2} is the mass fraction of oxygen in the air, and Q_{O_2}represents the mass per unit volume per unit time for oxygen consumption and was defined by Eq. (7):

$$Q_{O_2} = -(\phi_{GAC}\rho_{GAC})\,\nu_{O_2}R_{GAC} \tag{7}$$

where φ_{GAC} and ρ_{GAC} is the GAC porosity and density, respectively.

The conservation of energy considers local thermal non-equilibrium (LTNE), i.e., the temperature of the solid (T_s) differs from the temperature of the gas (T_g) [13, 29, 33]:

$$(\rho\, C_p)_{eff}\frac{\partial T_s}{\partial t} = \frac{1}{r}\frac{\partial}{\partial r}\left(rk_{eff}\frac{\partial T_s}{\partial r}\right) + \frac{\partial}{\partial z}\left(k_{eff}\frac{\partial T_s}{\partial z}\right) + h_{sg}\left(\frac{A_{s,sp}}{V_{sp}}\right)\left(T_g - T_s\right) + Q_{gen} \tag{8}$$

$$\phi_g\rho_g C_{P_g}\frac{\partial T_g}{\partial t} + \rho_g C_{P_g}(u_r\frac{\partial T_g}{\partial r} + u_z\frac{\partial T_g}{\partial z}) = \frac{1}{r}\frac{\partial}{\partial r}\left(r\phi_g k_g\frac{\partial T_g}{\partial r}\right) + \frac{\partial}{\partial z}\left(\phi_g\, k_g\frac{\partial T_g}{\partial z}\right) + h_{sg}(\frac{A_{s,sp}}{V_{sp}})(T_s - T_g) \tag{9}$$

where $A_{s,sp}$ and V_{sp} are the surface area and volume of the sand, respectively, and Q_{gen} represents the volumetric energy production rate from GAC oxidation (ΔH_{GAC}):

$$Q_{gen} = \phi_{GAC}\rho_{GAC}(\Delta H_{GAC}R_{GAC}) \tag{10}$$

The interfacial heat transfer coefficient (h_{sg}) between the solid and gas phases is based on an empirical Nusselt (Nu) versus Reynolds (Re) and Prandtl (Pr) correlation [56]:

$$Nu = \frac{h_{sg}\, d_p}{k_g} = 0.001\,(Re^{1.97}Pr^{1/3}) \tag{11}$$

Eq. (9) assumes effective thermal properties for solid phase [13]:

$$(\rho C_p)_{eff} = (\phi_s)(\rho_s C_{P_s}) + (\phi_{GAC})(\rho_{GAC}C_{P_{GAC}}) \tag{12}$$

$$k_{eff} = (\phi_s)(k_s + k_{rad}) + (\phi_{GAC})(k_{GAC}) \tag{13}$$

$$\phi_g = \phi - \phi_{GAC} \tag{14}$$

$$\varphi_s = 1 - \varphi \tag{15}$$

where ρ_s, ρ_{GAC}, ρ_g; ϕ_s, φ_{GAC}, ϕ_g; C_{P_s}, $C_{P_{GAC}}$, C_{P_g}; and k_s, k_{GAC}, k_g are the densities, porosities, heat capacities, and thermal conductivities of the sand, GAC, and gas, respectively. Radiative heat transfer was embedded in the effective solid conductivity following the Rosseland approximation ($k_{rad} = 16\sigma\, d_p T_s^3/3$) [56], where σ is the Stefan-Boltzmann constant [57]. Conductive heat transfer within the metal sheet was also modelled [23]:

$$(\rho_i \, C_{p_i}) \frac{\partial T_s}{\partial t} = \frac{1}{r} \frac{\partial}{\partial r}\left(r(k_i) \frac{\partial T_s}{\partial r}\right) + \frac{\partial}{\partial z}\left(k_i \frac{\partial T_s}{\partial z}\right) \quad (16)$$

where ρ_i, C_{p_i}, k_i are density, heat capacity and thermal conductivity of the metal sheet. The model parameters not described above are presented in Table 2 and the initial and boundary conditions are provided in Table 3. The heater was simulated by a constant heat flux (measured) delivered at the inlet boundary. The Darcy air flux was initiated at x=0 m by a constant $u_{g,in}$ (measured).

Table 2. Numerical Model Input Parameters

Parameters	Value	Unit	Ref
$log\ (A_{GAC})$	3.79	log(1/s)	This work
$C_{P_{GAC}}$	1100	J/ kg K	[58]
C_{p_i}	440.8	J/ kg K	[59]
C_{GAC}	0.03	-	This work
D_g	$4.35\ \times 10^{-5}$	m^2/ s	[60]
ΔH_{GAC}	-24.9	MJ/ kg	[30]
E_{GAC}	72.9	kJ/ mol	This work
H	7	W/ m^2 K^1	This work
k_{GAC}	0.25	W/ m K	[58]
k_i	14.7	W/ m K	[61]
k_p	1.4×10^{-9}	m^2	This work
m_s	10.019	kg	This work
m_{GAC}	0.301	kg	This work
M_g	28.97	g/mole	[62]
ϕ	0.442	-	This work
ϕ_{GAC}	0.05	-	This work
ρ_{GAC}	1311	kg/ m^3	This work
$\rho_{b_{GAC}}$	44.4	kg/ m^3	This work
ρ_i	8000	kg/ m^3	[63]
$\dot{q}$	22028±1053	W/m^2	This work
R	5.4	cm	This work
R_g	8.314	J/ mol K	[56]
$u_{g,in}$	0.05	m/s	This work
ν_{O_2}	2.304	kg. O_2/ kg. fuel	[30]
ν_{co}	0.63	kg. CO/ kg. fuel	[30]
ν_{co_2}	2.67	kg. CO_2/ kg. fuel	[30]
σ	5.67×10^{-8}	W/m^2 K^4	[56]

Table 3. Initial and Boundary Condition in Numerical Simulation

Eq.	Initial Condition ($t = 0$)	Boundary Condition
(3)	$Y_{GAC} = 1$	$z = 0 \,\&\, 0 < r < 0.054 \rightarrow \begin{cases} -(k_s + k_{rad})\dfrac{\partial T_s}{\partial z} = \dot{q} \rightarrow 0 \le t \le t_h \\ -(k_s + k_{rad})\dfrac{\partial T_s}{\partial z} = 0 \rightarrow t_h \le t \le t_f \\ T_g = T_0 \\ \rho_g u_g = \rho_g u_g(t) \begin{cases} u_g = 0 \rightarrow 0 \le t \le t_g \\ u_g = u_0 \rightarrow t_g \le t \le t_f \end{cases} \\ Y_{O_2} = Y_{O_2,0} \end{cases}$
(4)	$P = 101375$ Pa	$z = 0 \,\&\, 0.054 < r < 0.057 \rightarrow \begin{cases} -(k_i)\dfrac{\partial T_s}{\partial z} = \dot{q} \rightarrow 0 \le t \le t_h \\ -(k_i)\dfrac{\partial T_s}{\partial z} = 0 \rightarrow t_h \le t \le t_f \end{cases}$
(6)	$Y_{O_2} = 0.23$	$z = 0.76 \,\&\, 0 < r < 0.054 \rightarrow \begin{cases} -(k_s + k_{rad})\dfrac{\partial T_s}{\partial z} = 0 \\ -(k_g)\dfrac{\partial T_g}{\partial z} = 0 \\ P_g = P_0 \\ -(D_g)\dfrac{\partial(\rho_g Y_{O_2})}{\partial z} = \rho_g u_g(Y_{O_2,0} - Y_{O_2}) \end{cases}$
(8-9)	$T_s = T_g = 295\,K$	$r = 0 \,\&\, 0 < z < 0.76 \rightarrow \begin{cases} -(k_s + k_{rad})\dfrac{\partial T_s}{\partial r} = 0 \\ -(k_g)\dfrac{\partial T_g}{\partial r} = 0 \\ -(D_g)\dfrac{\partial(\rho_g Y_{O_2})}{\partial r} = 0 \\ u_r = 0 \end{cases}$
(8)	$T_s = 295\,K$	$z = 0.76 \,\&\, 0.054 < r < 0.057 \rightarrow \left\{ -(k_i)\dfrac{\partial T_s}{\partial z} = 0 \right.$
(16)	$T_s = 295\,K$	$r = 0.057 \,\&\, 0 < z < 0.76 \rightarrow \left\{ -(k_i)\dfrac{\partial T_s}{\partial r} = H(T_s - T_\infty) \right.$

The effective radial heat loss coefficient (H) was determined by a sensitivity analysis (Supplementary Material, Section B) based on an established methodology [29]. In this work, H is the only model parameter not independently known and represents the radial heat losses at the outer surface of the column wall (Fig. 1). H is further introduced in the Supplementary Material, Section B.

Table 4 shows the equations for a new global energy balance in two-dimensions based on the approach developed by [16, 22]. The energy rates at inlet (heat influx, $\dot{E}_{in}$) and the outlet (convective outflux, $\dot{E}_{out}$) were calculated by integrating the energy fluxes over the column radius. The radial heat loss rate ($\dot{E}_{loss}$) was integrated over the column outer surface area and the oxidation rate ($\dot{E}_{oxi}$) was integrated over the column volume. The net energy rate ($\dot{E}_{net}$) corresponds to the sum of these four components (Eq. 21). The integral over time of the energy rates results in the net energy (E_i) associated with each component j.

Table 4. The Rate and Accumulation of Energy

Energy	Eq.	
Rate of cone heater	$\dot{E}_{in} = \int_0^R \dot{q}\ 2\ \pi\ \mathrm{r}\ \mathrm{dr}$	(17)
Rate of GAC oxidation	$\dot{E}_{oxi} = \iint_0^{R,L} -\Delta H_{GAC}(\phi_{GAC}\rho_{GAC})R_{GAC}\ \ 2\ \pi\ r\ dr\ dz$	(18)
Rate of radial heat loss	$\dot{E}_{loss} = \int_0^L H\ (T_{s_{(r=R)}} - T_\infty) 2\ \pi\ \mathrm{R}\ \mathrm{dz}$	(19)
Rate of convective hot air	$\dot{E}_{out} = \int_0^R (\rho_g u_g)\ C_{p_g} \left(T_{g_{(z=0.74)}} - T_\infty\right) 2\pi\ r\ dr$	(20)
Rate of net	$\dot{E}_{net} = \dot{E}_{in} + \dot{E}_{oxid} - \dot{E}_{out} - \dot{E}_{loss}$	(21)
Accumulation	$E_j(t) = \int_0^t \dot{E}_j dt$	(22)
Accumulation of net	$E_{net}\ (\mathrm{t}) = E_{in}(\mathrm{t}) + E_{oxid}(\mathrm{t}) - E_{out}(\mathrm{t}) - E_{loss}(\mathrm{t})$	(23)

A multi-dimensional global energy balance [16] was performed to determine System Energy Efficiency (SEE) which normalize the effects of heat losses against the energy generated, following the approach of [29]:

$$\text{System Energy Efficiency} = \frac{E_{net}(t)}{E_{net,adiabatic}(t)} \sim \frac{E_{oxi}(t) - E_{loss}(t)}{E_{oxi}(t)} \tag{24}$$

where $E_{net,adiabatic}(t)$ was estimated by assuming a perfectly insulated column ($H = 0\, W/m^2K$). Moreover, Eq. (24) assumes that the net accumulated energy (Eq. 23) is dominated by $E_{oxi}(t)$ and $E_{loss}(t)$, since $E_{in}(t)$ is an initial effect and is negligible compared to the energy added through smouldering. Then, a SEE sensitivity analysis was conducted by changing the radius of column (R) and heat loss coefficient (*H*). Model simulations were compared with published studies showing: (i) analytical [29], (ii) numerical [22, 23], and (iii) experimental [26, 30] results.

2.2 Experiments

This work conducted 3 experiments (with 3 repeats each, nine total) to provide a robust, unique data set for 2D heat transfer as well as 2D smouldering. Figure 2 shows a schematic of the experimental setup. The smouldering experiments (Table 5) were carried out in a stainless-steel column (316 Stainless Steel) with a 1 cm layer of clean sand and a 75 cm layer of sand/GAC, topped by a 9 cm layer of a clean sand. The heat transfer experiments used the same setup, but only used clean sand (i.e., no GAC). GAC is a by-product of coal pyrolysis and was chosen as a model fuel because it minimizes chemical complexity [13, 25, 30, 48, 49]. The column was wrapped in a 4 cm insulation layer (Superwool plus, Morgan Thermal Ceramics) and enclosed by an aluminum jacket to hold the insulation in place.

Table 5. Experimental Test Specifications

Exp. # (-)	GAC Concentration (C_{GAC})	Repeats (-)	Heater Stabilization Time (t_{stab}) [s]	Air on Time (t_g) [s]	Heater off Time (t_h) [s]
1	0	3	470	1023	2400
2	0.02	3	660	1020	4320
3	0.03	3	632	3655	4380

The thermocouples (Type K, Inconel, Omega) were placed at (i) the centerline spaced 3 cm apart and (ii) radially from 13 to 61 cm, spaced 12 cm apart (see the position of the thermocouples, Fig. 2). Temperatures were recorded every two seconds by a data logger (Multifunction Switch/Measure Unit 34980A, Agilent Technologies). The sand (K&E Sand and Gravel, WP #2) was sieved to achieve a grain size between 0.118 and 0.200 cm. GAC (McMaster-Carr, CAS Number: 7440-44-0 particle size between 0.425 and 0.85 mm) was combined with sand at 0.02 and 0.03 kg/kg sand using an electric mixer (Kitchen Aid), and then carefully packed in the column to ensure good homogeneity. The intrinsic permeability of the bed was measured in the column (k_p) [56, 64, 65] and did not change after smouldering; unsurprising since the fuel load was so minor (i.e., 2% to 3% of the fuel bed by mass; see Supplementary Material, Section A). An external radiative cone heater (500 W, 240 V, Fire Testing Technology Ltd.) was placed below the column. The heater temperature was set to 1000 °C, providing the heat flux required for smouldering ignition. The heat flux ($\dot{q}$) from the heater towards the column inlet boundary was measured using a High Temperature Heat Flux Sensor (HTHFS-01, FluxTeq) attached to a quartz window (Esco product Inc.) placed at the bottom of the column (Fig. 2). See additional information on this measurement in the Supplementary Material, Section A.

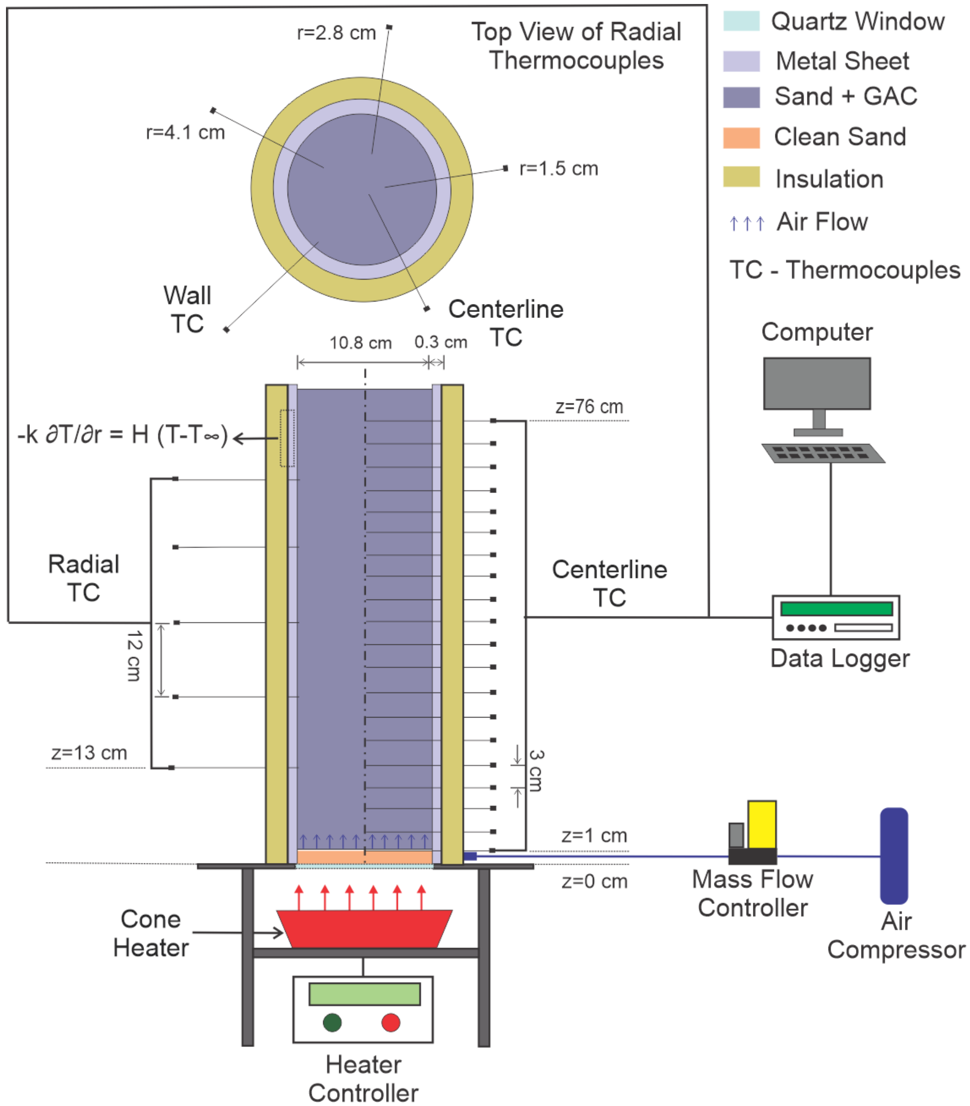

Figure 2. Schematic view of experimental setup. For smouldering experiments, the contaminated region (sand mixed with GAC) is represented by the gray layer. For heat transfer experiments, the contaminated region is fully replaced by clean sand (orange layer).

Table 5 shows the experimental conditions, which all followed a standard procedure [13]. The heater was turned on and stabilized at 1000 °C at t_{stab}, i.e., the time when the thermocouple at specific height above the heater (i.e., 1 cm and 4 cm in the heat transfer-only and smouldering experiments, respectively) reached 300 °C. The air supply was turned on at t_g, thereby causing ignition in the smouldering experiments, and the Darcy flux ($u_{g,in}$) was controlled via a mass flow controller (FMA5400 Series, 0-80 L min-1, Omega Ltd). The heater was turned off at t_h (i.e., when the thermocouple 4 cm and 7 cm above the heater peaked in the heat transfer-only and smouldering experiments, respectively), while the air was kept on until the end of the experiment (see Fig. B1, Supplementary Material, Section B). To directly compare the results from smouldering experiments and simulations, parameters including temperature, air mass flux, GAC bulk density, and oxygen mass fraction were normalized in Table 6. The time also was normalized to a Dimensionless Time (DT) [16] to account for differences in the smouldering front velocities and ignition times [64].

Table 6. Dimensionless Parameters used in Smouldering Experiments and Simulations

Parameter	Eq.	
Time	$DT = \frac{(t - t_g)v_f}{L}$	(26)
Solid Temperature	$DT_s = \frac{T_s}{T_{s_p}}$	(27)
Air Mass Flux	$D\rho u_g = \frac{\rho\, u_g}{(\rho\, u_g)_{in}}$	(28)
GAC Bulk Density	$D\rho_{b_{GAC}} = \frac{\rho_{b_{GAC}}}{(\rho_{b_{GAC}})_0}$	(29)
Oxygen Mass Fraction	$DY_{O_2} = \frac{Y_{O_2}}{(Y_{O_2})_{in}}$	(30)

where v_f is the average smouldering front velocity (calculated using the procedure from [66]) and L is the length of the packed bed. $DT < 0$ represents the pre-heating period before air injection (i.e., when conduction and radiation dominated); $DT = 0$ signals the beginning of air injection and smouldering ignition (i.e., when the temperature near the heater rapidly increases due to the energy released by oxidation); and $0 < DT \leq 1$ represents the smouldering propagation time, where $DT = 1$ is the time when smouldering reached the top of the column and the reaction finished. Other parameters are also explained in Table 2.

3. Results and Discussion

3.1 Quantitative Analysis of Multi-dimensional Smouldering

3.1.1 2D Heat Transfer Model

Figure 3 compares the heat transfer-only experiments and simulations. This figure shows excellent agreement between the experimental and simulated temperature evolutions with errors of 6% and 7% at the centerline and wall, respectively. When the heater was turned on, the temperatures increased by conduction and radiation. Then, the air supply was turned on and convection drives heat transfer. As the heat wave progresses upwards, it is dissipated axially (due to axial convection) and radially (due to heat losses). The radial boundary condition applied to the simulations in Fig. 3 used H = 1.8 W/m^2 K which agrees with [29].

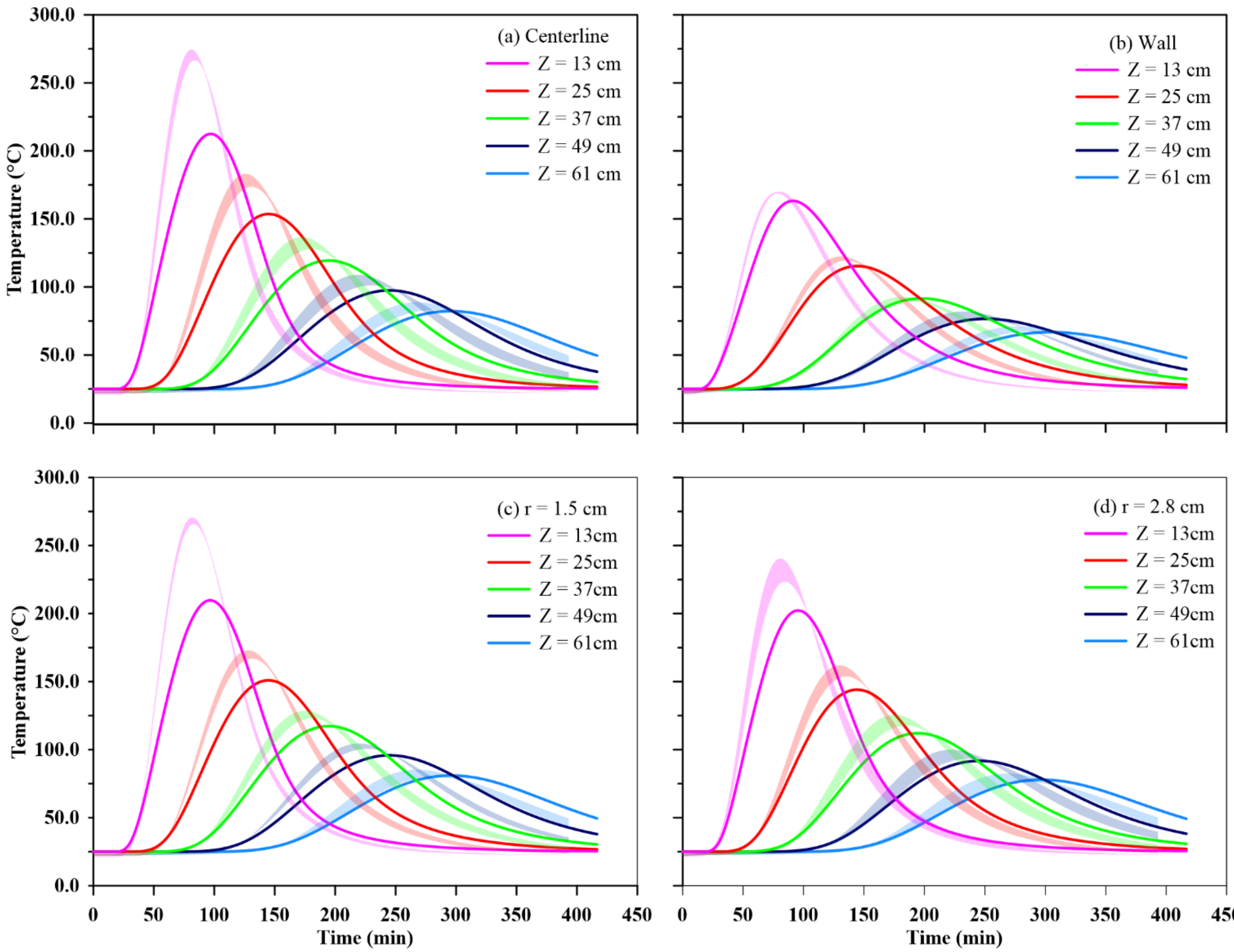

Figure 3. Temperature evolution for the heat transfer experiments and simulation along various radial positions: a) centerline, b) wall, c) r = 1.5 cm, and d) r = 2.8 cm. The solid lines represent numerical results and the shaded region shows 95% confidence interval of experimental results.

3.1.2 2D Smouldering Model

Figure 4 includes the complexity of GAC smouldering revealed by the numerical model. Like Fig. 3, Fig. 4 also shows excellent agreement between GAC smouldering (0.03 kg GAC/kg sand) experiments and numerical results at the centerline (error = 5%, Fig. 4a), wall (error = 8%, Fig. 4b), r = 1.5 cm (error = 5%, Fig. 4c), and r = 2.8 cm (error = 7%, Fig. 4d). The peak temperatures (T_p) were quite constant along the column, where the average centerline T_p was 732 ± 6 °C (experimental) and 718 °C (numerical) and the average wall T_p was 609 ± 23 °C (experimental) and 480 °C (numerical). The temperature difference between experimental and numerical results at the wall are likely associated with wall effects that were not completely captured by the numerical model. That is, the wall boundary condition only approximated the thermal resistance offered by the insulation and did not model all thermophysical properties in the wall materials (i.e., surrounding insulation), for computational efficiency. A sensitivity analysis of the heat loss coefficient (H) resulted in H = 7 W/m^2 K, which is within the range expected due to free convection [67]. Further discussion is included in the Supplementary Material, Sections B. Although slight differences between model results and experiments at the wall, the model was able to accurately reproduce the key trends governing the multi-dimensional interplay between heat transfer mechanisms and chemical reactions during smouldering.

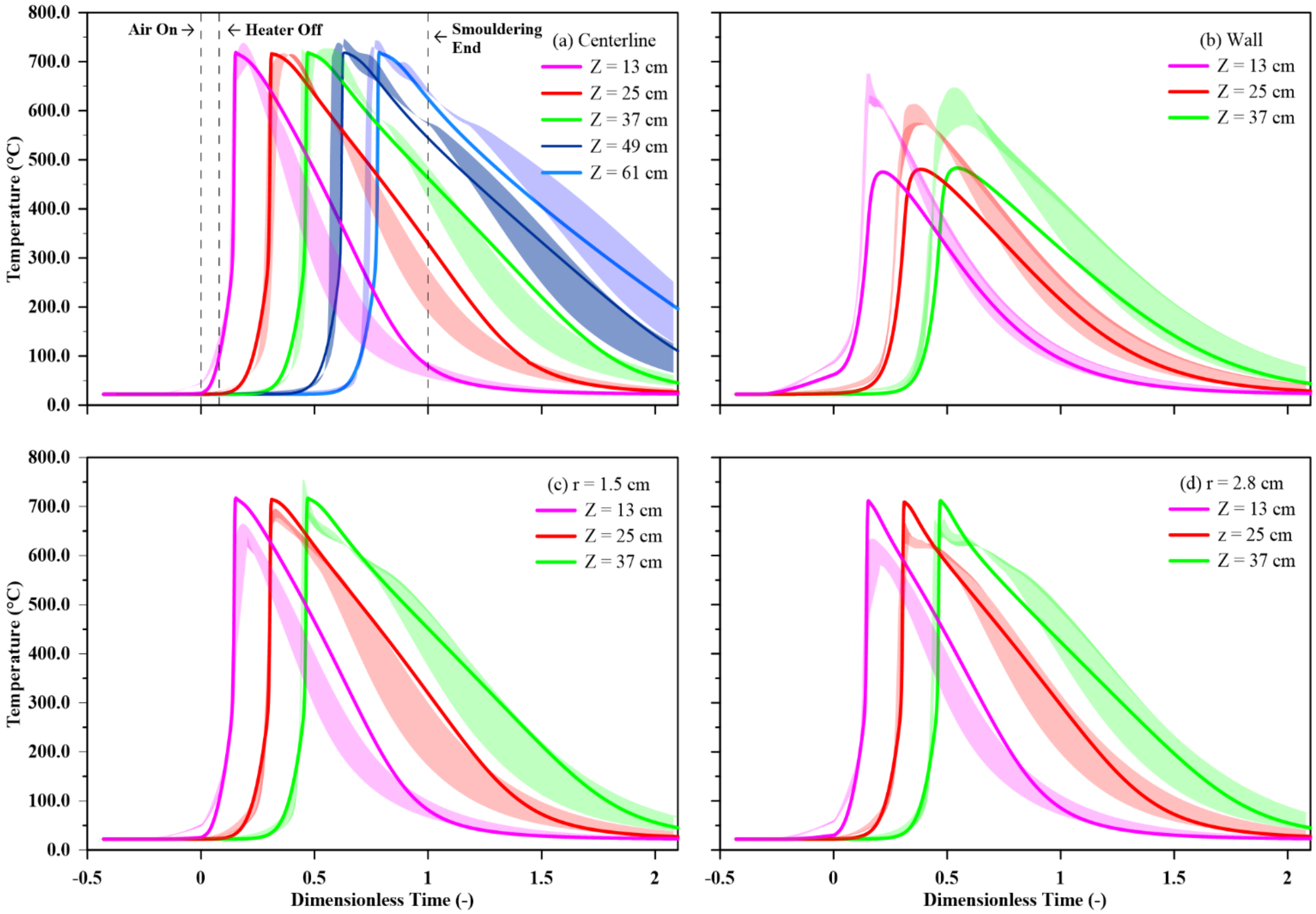

Figure 4. Temperature evolution at multiple radial positions: a) centerline, b) wall, c) r = 1.5 cm, and d) r = 2.8 cm. The solid lines represent numerical results and the shaded region shows 95% confidence interval from experimental results (i.e., three repeats).

While Fig. 4 focused on the good matching in the transient smouldering behaviour, Fig. 5 illustrates that the key spatial trends were also well-simulated. Figure 5a shows excellent agreement between experimental and numerical peak temperatures 37 cm from the heater (i.e., away from inlet and outlet boundary effects). The temperature distribution shows a convex smouldering front, with lower temperatures at the wall, as expected due to radial heat losses [23, 26, 68]. Figure 5b also shows a good agreement for the centerline longitudinal temperature distribution between experiments and simulations at three dimensionless times: DT = 0.25, 0.50, and 0.75. These results show that the model is capable of reproducing: (*i*) the pre-heating ahead of the front (which validates the effective thermal properties used), (*ii*) the position of the smouldering front (which validates the simple one-step oxidation reaction and agrees with [29]), and (*iii*) the temperature cooling behind the front (which validates the approach used for simulating heat losses).

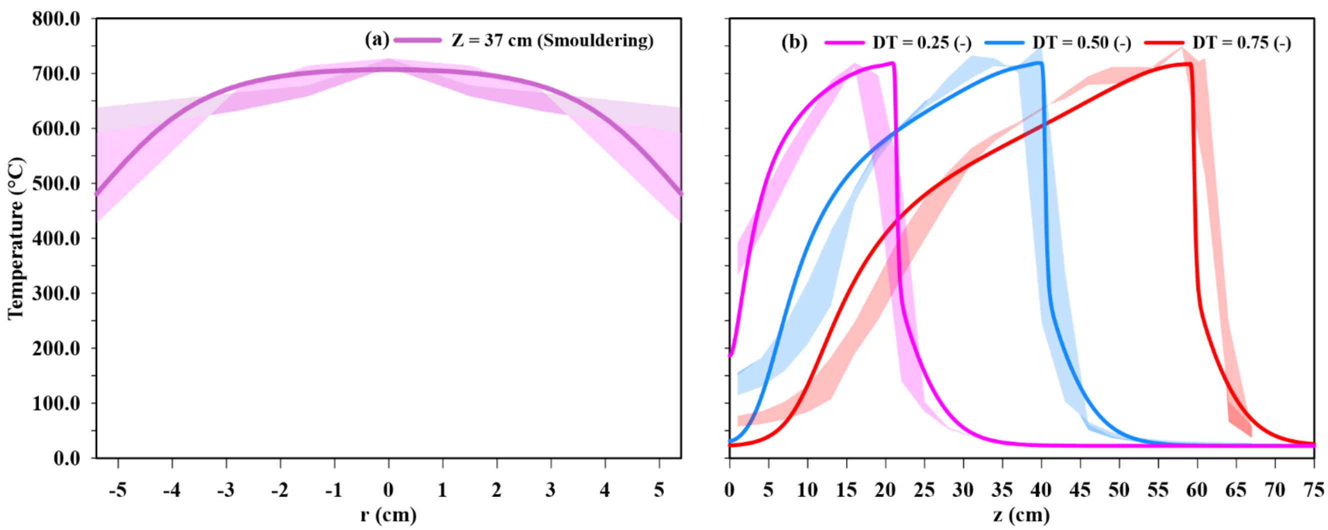

Figure 5. a) Radial peak temperature distribution at 37 cm comparing experimental (shaded region) and numerical (solid line) results, b) Centerline temperature distribution along the length of the column at 3 different DT: 0.25, 0.50, and 0.75.

3.1.3 Quantitative Model Validation

The robustness of the model in predicting experiments was tested in Fig. 6. The complete temperature profiles from these simulations and results can be seen in the Supplementary Materials, Section B, which align with the results presented above in Fig. 4. Figure 6 compares the average peak temperature (T_p) and smouldering front velocity (ν_f) for different GAC concentrations from 0 (i.e., heat transfer-only) to 0.03 kg GAC/kg sand. Both the peak temperature and front velocity increase with GAC concentration as more GAC drives hotter, faster smouldering. By increasing GAC concentration from 0 to 0.03, radial heat transfer coefficient (H) increases from 1.8 to 7.0 W/m^2 K (determined using sensitivity analysis, Supplementary Material, Section B). This increase is because: (*i*) the higher temperatures experienced during smouldering with higher GAC concentration should foster greater heat losses due to differences in the thermophysical properties of insulation (e.g., higher thermal conductivity) and (*ii*) the mechanism of radial heat transfer from column wall to the ambient air is free convection heat transfer, which should also increase with the wall temperature [67]. The model validation was accomplished by comparing the experimental and numerical peak temperatures and smouldering front velocities, respectively, which demonstrate excellent agreement: 658 ± 14 (experimental) and 617 ºC (numerical) and 0.36 ± 0.07 (experimental) and 0.37 cm/min (numerical).

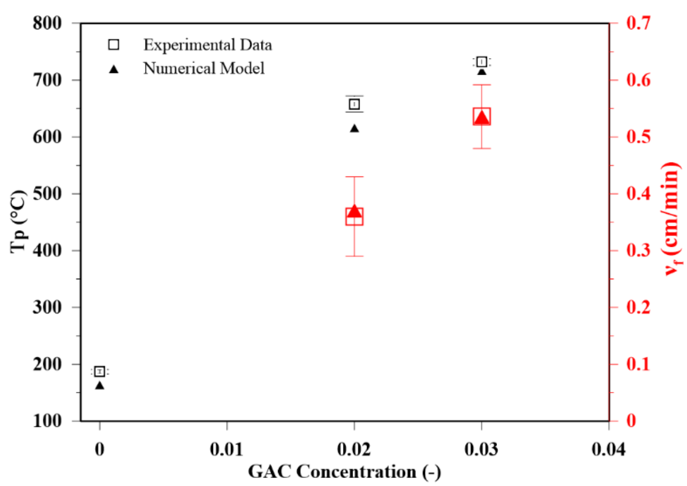

Figure 6. Peak Temperature (T_p) and smouldering front velocity (ν_f) versus GAC concentration.

3.1.4 Global Energy Balance

In further understanding the implications of smouldering system behaviour, Fig. 7 shows a multi-dimensional global energy analysis (see the equations in Table 4). During the preheating time ($DT < 0$), the energy rate leaving the system by radial losses ($\dot{E}_{loss}$) is less than the rates of energy entering the system through the heater ($\dot{E}_{in}$) and released by oxidation ($\dot{E}_{oxi}$), i.e., $\dot{E}_{loss} < \left(\dot{E}_{in} + \dot{E}_{oxi}\right)$, Fig. 7a. Note that, while the air supply is off during this period, oxidation is weakly activated by the initial oxygen present inside the pores. Therefore, the net energy rate ($\dot{E}_{net}$) is positive and energy accumulates (E_{net}) in the system, Fig. 7b. When the air supply is turned on ($DT = 0$), the oxidation energy rate ($\dot{E}_{oxi}$) is fully activated and remains nearly constant until total fuel consumption at end of smouldering ($DT = 1$). Moreover, $\dot{E}_{loss}$ increases due to the increasing length of the cooling zone (hot clean sand), which increases the surface area for radial heat losses (approximately 52 and 70% of the energy added into the system is lost radially when smouldering with 0.02 and 0.03 GAC concentration, respectively, agreeing with [26]). However, the energy leaving the system through the outlet ($\dot{E}_{out}$) is negligible when $DT < 1$ (as the exiting emissions are nearly at ambient temperatures). While $\dot{E}_{in}$ is crucial for ignition, the heater is turned off early in the simulation ($DT = 0.08$); therefore, $\dot{E}_{in}$ is negligible throughout most of smouldering. Thus, the global energy balance is governed by a balance between $\dot{E}_{loss}$ and $\dot{E}_{oxi}$. Since $\dot{E}_{net}$ is strongly positive, the system rapidly accumulates energy as smouldering proceeds in a self-sustaining manner. When smouldering is finished ($DT > 1$), energy starts leaving the system ($\dot{E}_{net} < 0$) via $\dot{E}_{out}$, and E_{net} decreases to ambient values. The numerical error associated with spatial and temporal discretization was calculated via the global energy balance and was approximately 2%. Altogether, these results show expected behaviour, but improve upon previous global energy developments by resolving all terms in a fully-coupled, multi-dimensional model.

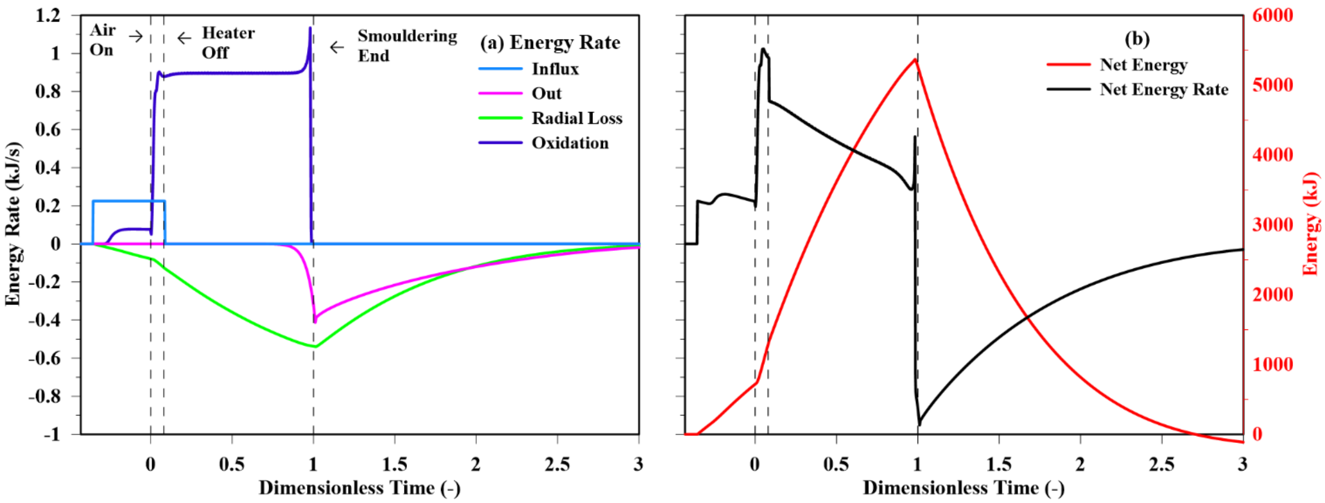

Figure 7. a) Energy rate for inlet, outlet, loss, and oxidation, b) net cumulative energy and energy rate.

3.1.5 Quantitative Model Verification

Figure 8 presents the results from a System Energy Efficiency (SEE) analysis (i.e., previously developed by [29] and presented in Eq. 24). In this analysis, the radial heat losses depend on the radius of the column (R) and heat loss coefficient (H) and approximate all terms when the smouldering front travelled 33 cm (i.e., a propagation distance common to many experimental and numerical smouldering studies). Therefore, a sensitivity analysis with a series of numerical and analytical simulations was performed by changing R and H. Figure 8 shows that the numerical results are in excellent agreement with the analytical solutions when $R > 10$ cm. This provides a robust verification of the numerical model. Additionally, the numerical model predictions are in good agreement with previous experimental and numerical studies, which provides extra confidence in the model's predictive capacity over these system conditions [22, 23, 26, 29].

Figure 8 also reveals that by decreasing H and increasing R (decreasing surface-area-to-volume ratio), the SEE improves (agreeing with [29]) due to the diminishing influence of radial heat losses. Moreover, simulations show that for $R > 40$ cm, the SEE is insensitive to both R and H. However, the analytical model diverges from the numerical simulations with $R < 10$ cm (i.e., the shaded region in Fig. 8). This divergence is due to different assumptions during quenching, where the numerical simulations more accurately capture the global energy balance terms at conditions near quenching than the approximations embedded in the analytical model [29].

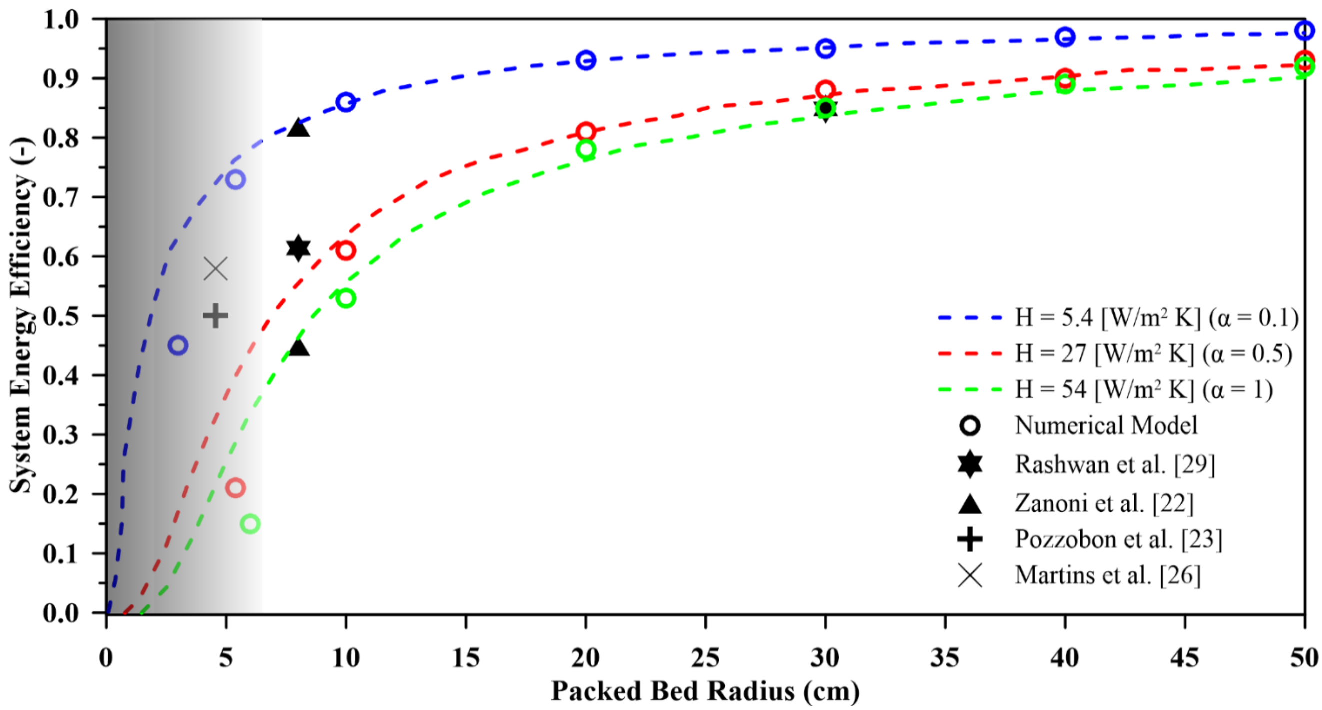

Figure 8. System energy efficiency predicted by the calibrated numerical model (coloured circles), analytical model (coloured, dashed lines), and previous studies (symbols) from Rashwan et al. [29], Zanoni et al. [22], Pozzobon et al. [23], and Martins et al. [26]. Different radius (from 4 to 50 cm) and different heat loss coefficients (from 5.4 to 54 W/m^2 K) were considered. Increasing H represents decreasing the quality of insulation. The shaded gray region shows where the analytical predictions are less accurate because of quenching effects.

3.2 Qualitative Analysis of Multi-dimensional Smouldering

3.2.1 Qualitative Model Validation

2D contour maps and videos of the solid temperature, GAC bulk density, and oxygen mass fraction are presented in Fig. 9. Figures 9a and 9b compare 2D contours of the experimental and numerical solid temperatures, respectively, at DT = 0.5. These figures reveal similar temperatures and positions and shapes of the cooling front, smouldering front, and pre-heating zone. The slight differences are related to the low experimental temperature resolution. Moreover, Fig. 9b shows non-uniform air flux. This air flow divergence decreases the air mass flux from 0.059 kg/m^{2}s at the inlet boundary to ~0.055 kg/m^{2}s at the centerline, while it increases air mass flux to 0.082 kg/m^{2}s near the wall.

Three different zones shown in Fig. 1 are determined in Fig. 9a, as previously seen in [33]. Region (I) notes the end of the cooling zone, which is governed by convection heat transfer between hot clean sand and inlet cold air from inlet. This region grew to ~13 cm in Figs. 9a and 9b. The shape of the cooling front in this region is concave (i.e., higher temperature at the wall), as a fraction of the energy released from smouldering was transferred quickly downward along the highly conductive wall into this region. Region (II) shows the remaining length of the cooling zone, which grew to ~23 cm in Figs. 9a and 9b. Similar to Region (I), Figs. 9a and 9b show that the numerical model captured the major trends in Region (II) observed in the experiment. This region is controlled by the difference between the smouldering and cooling velocities and distorted by radial heat losses. Without radial heat losses, this region would grow indefinitely; however, with heat losses, it would reach a maximum length when the radial heat losses balance the rate of energy released from smouldering. In this region, the temperatures were higher at the centerline due to radial heat losses [16, 29]. Region (III) shows the smouldering front associated with GAC oxidation, which was ~0.15 cm thick at DT = 0.5. Figure 9c shows that GAC was fully destroyed, and only clean sand remained behind the smouldering front. These smouldering front features agree with many applied smouldering studies, e.g., [14, 23, 26, 65, 69]. Moreover, the smouldering front is convex (higher temperatures at the centerline), which agrees with the simulations from [23] under similar conditions. Unlike the fuel in this region, the oxygen is not fully consumed, i.e., it decreases from 0.23 to 0.06 and 0.12 at the centerline and wall, respectively. Higher oxygen consumption at the centerline fosters more robust chemical reactions, which contributed to higher peak temperatures. Finally, Region (IV) shows the pre-heating zone, where the temperature of the sand/GAC layer is increased by the hot air passing through the smouldering front. It was hypothesized that there is a superadiabatic effect associated with local radial velocity component that brings heat towards the centre from wall [25]. These numerical results provide quantitative results that substantiate that hypothesis.

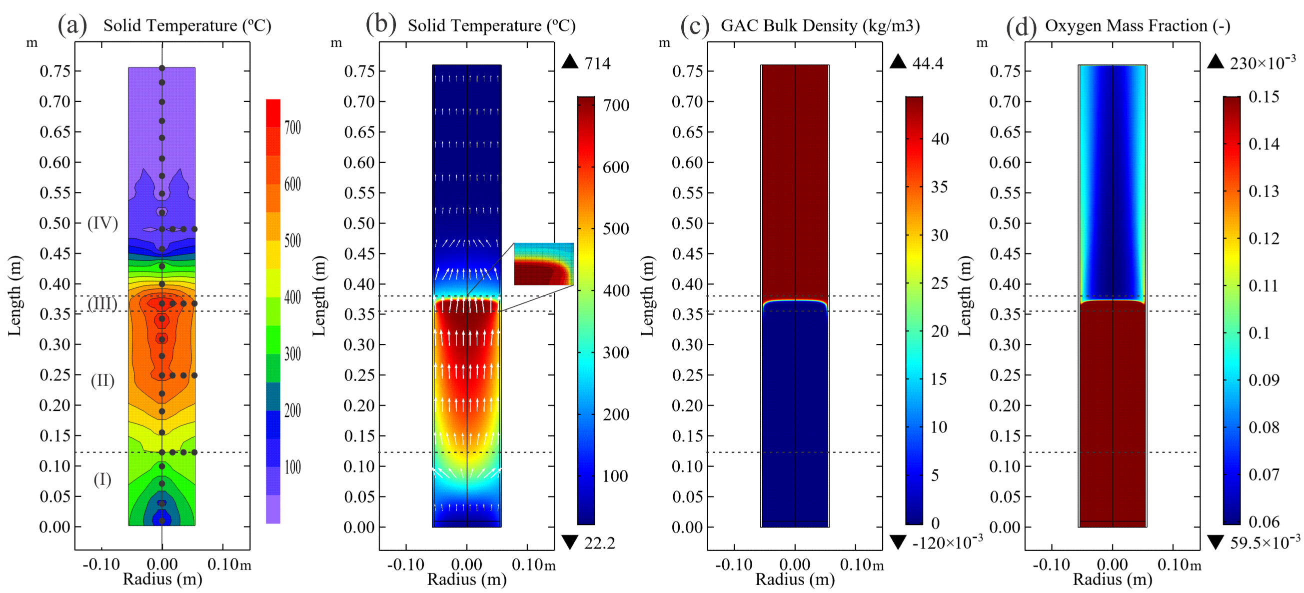

Figure 9. 2D contours of: (a) experimental temperatures (Video S1. a), (b) simulated solid temperature (Video S1. b), (c) simulated GAC bulk densities (Video S1. c), and (d) oxygen mass fractions (Video S1. d).

3.2.2 Qualitative Analysis of Non-Uniformities

Figure 10 shows a model simulation of GAC smouldering with 0.02 kg GAC/kg sand and H = 28 W/m^2 K. The non-uniformities of dimensionless parameters including solid temperature, air mass flux, GAC bulk density, and oxygen mass fraction were investigated (see Table 6). The results are shown in three different times including DT = 0 (i.e., smouldering initiation), 0.25 (i.e., peripheral extinction), and 0.50 (i.e., global quenching). Figures 10b, 10f, and 10j show peak temperatures drop near the wall due to radial heat losses in the cooling zone that lead to peripheral extinction at the initial time, agreeing with [15, 70], and global quenching at the latter time (i.e., non-self-sustaining smouldering), agreeing with [31]. Peripheral extinction fosters an unburned crust along the reactor wall that is cooler and facilitates air channeling; therefore, non-uniform air mass flux increases from centerline to the wall, agreeing with experimental data [23, 26, 38]. This non-uniformity is low initially (e.g., 0.78 to 1.43) then increases (e.g., 0.62 to 1.62) and, finally by quenching the smouldering, reduces again (e.g., 0.72 to 1.28); see Figs. 10a, 10e, 10i. The longitudinal distribution of air mass flux (Fig. 10m) shows minimum air mass flux at the centerline in the position close to the peak temperature where it tends to move around the hot zone towards the wall that causes a reduction in forward heat transfer at the centerline.

Figures 10c, 10g, and 10k show 2D contours of the GAC bulk density distributions, which show how chemical reaction non-uniformities develop in less robust smouldering systems (e.g., with lower SEE because of high heat loss coefficient (H) and low radius (R)). Peripheral extinction starts at early time then grows into the reactor center and leads to global quenching. A convex shape of the smouldering front is predicted, agreeing with the field data in [27], which confirms that, in this scenario, the effect of non-uniform reactions dominates that of non-uniform air mass flux [25]. Figures 10d, 10h, and 10l show 2D contours of the oxygen mass fraction distribution, where the oxygen supply decreases at the centerline because of non-uniform air flux that causes lower smouldering robustness. By decreasing the smouldering robustness, oxygen mass fraction consumption at the smouldering front drops, decreasing from 1 to 0.63

and 0.72 at DT = 0 and 0.25, respectively (see Fig. 10o). Altogether, Fig. 10 demonstrates the powerful capabilities of this novel multi-dimensional model in exploring many complicated and interconnected phenomena.

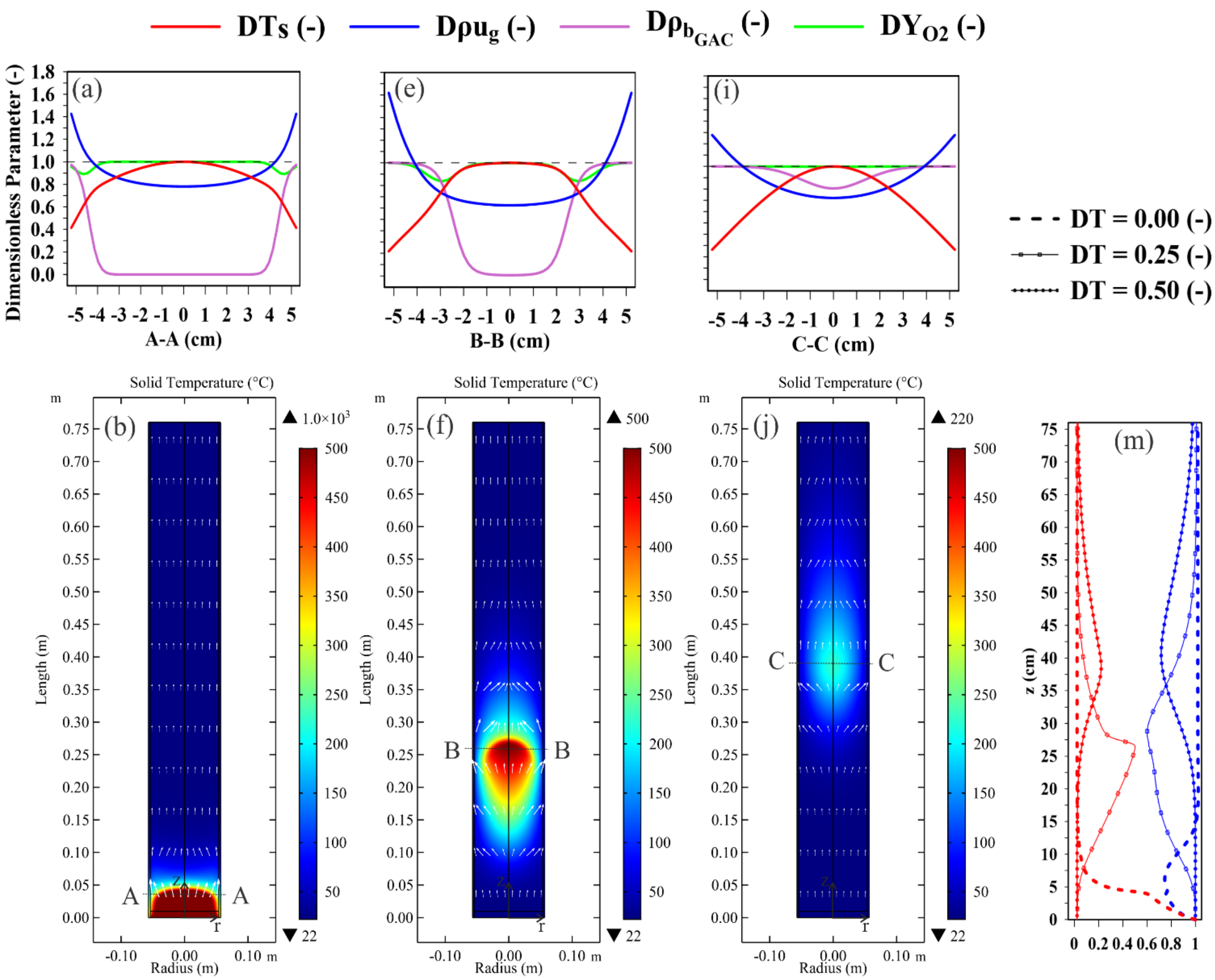

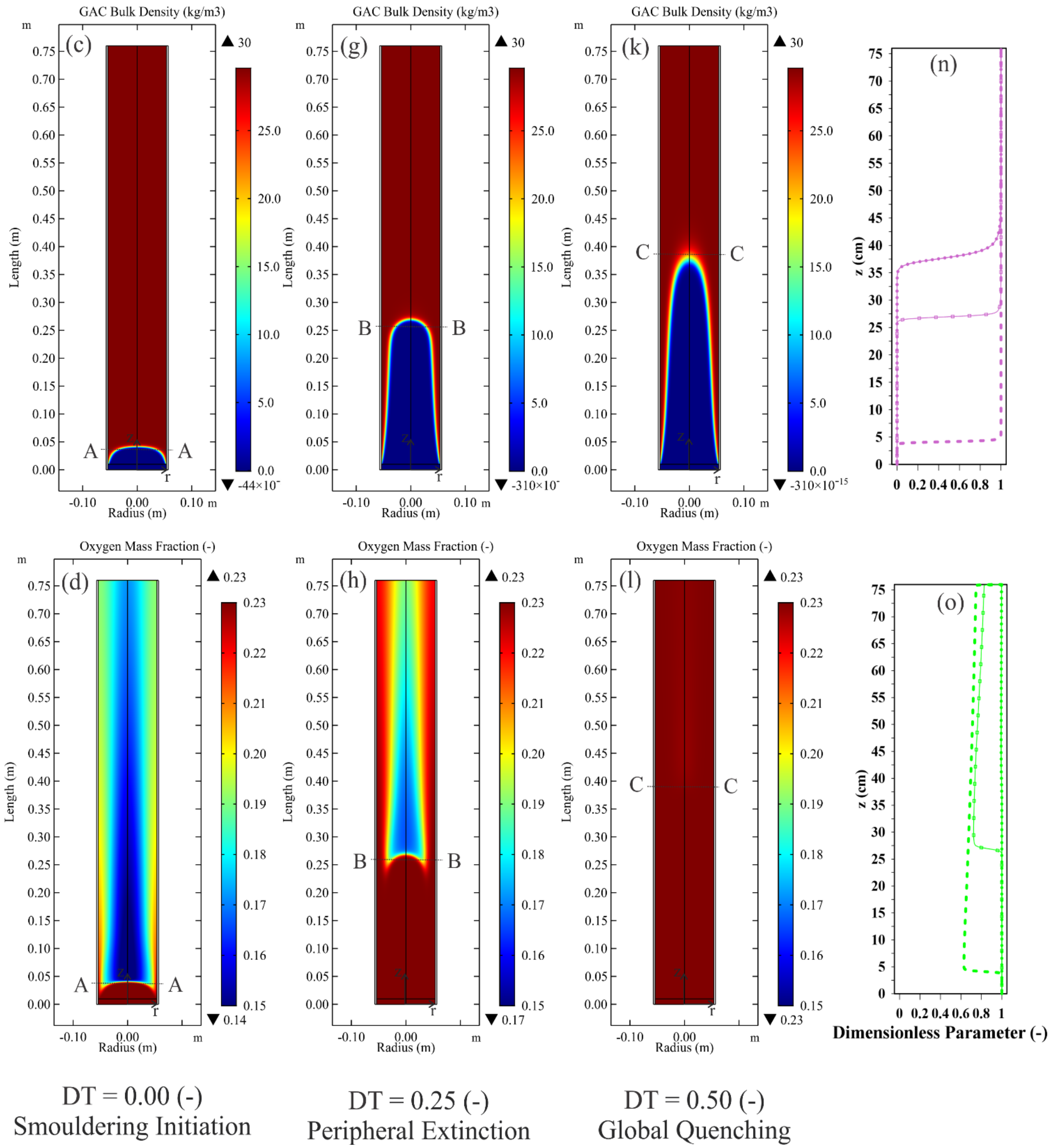

Figure 10. (a, e, and i) and (m, n, and o) show radial and longitudinal distribution of dimensionless parameters, respectively. 2D contours of temperature and air mass flux were shown in (Figs. b, f, and j), GAC bulk density (Figs. c, g, and k), and oxygen mass fraction (Figs. d, h, and l) at DT = 0.00, 0.25, and 0.50, respectively.

4. Conclusions

In this study, a 2D numerical model was developed and validated with experimental results quantitatively and qualitatively to investigate the effect of radial heat loss on temperature, air mass flux, oxygen mass fraction and chemistry distribution. For validating the 2D numerical model, a heat transfer model was developed by eliminating the effect of chemical reactions and then validated with heat transfer-only experiments. A simplified chemical model (i.e., global one-step oxidation reaction) achieved from TG/DTG experiments was proposed to describe GAC smouldering in an inert porous medium. Last, a 2D smouldering model was developed combining the heat transfer and chemical models.

The model predictions were in excellent agreement with the experimental results in terms of temperature evolutions in space and time, smouldering velocities, and the shape of smouldering front. The model also reproduced expected dynamics in non-uniform air mass flux and reactions. Moreover, it is perhaps the first model to accurately simulate both local and global extinction of smouldering across a range of scenarios. Therefore, this new model is anticipated to accurately predict smouldering behaviour over a wide range of conditions and is relevant for application and design. Furthermore, a global energy balance revealed evolutions in the overall system behaviour, and the results compared well with other energy balance results from numerical simulations, experiments, and analytical modelling in the literature. This clearly demonstrates the model's ability to capture the main physics and chemistry of smouldering and their complex interactions which significantly impact the outcomes. Altogether, this validated multi-dimensional smouldering model is anticipated to help better understand, design, and optimize future applied smouldering systems.

Acknowledgements

Funding was provided by the Natural Sciences and Engineering Research Council of Canada (Grant Nos. CREATE 449311-14, RGPIN 2018-06464 and RGPAS-2018-522602).

5. References

[1] H. Peng, H. Dong, X. Ling, Thermal investigation of PCM-based high temperature thermal energy storage in packed bed, Energy Conversion and Management 81 (2014) 420-427. https://doi.org/https://doi.org/10.1016/j.enconman.2014.02.052.

[2] M. Cascetta, G. Cau, P. Puddu, F. Serra, A comparison between CFD simulation and experimental investigation of a packed-bed thermal energy storage system, Applied Thermal Engineering 98 (2016) 1263-1272. https://doi.org/https://doi.org/10.1016/j.applthermaleng.2016.01.019.

[3] M. Hamidi, V.M. Wheeler, X. Gao, J. Pye, K. Catchpole, A.W. Weimer, Reduction of iron–manganese oxide particles in a lab-scale packed-bed reactor for thermochemical energy storage, Chemical Engineering Science 221 (2020) 115700. https://doi.org/https://doi.org/10.1016/j.ces.2020.115700.

[4] H.K. Wyn, M. Konarova, J. Beltramini, G. Perkins, L. Yermán, Self-sustaining smouldering combustion of waste: A review on applications, key parameters and potential resource recovery, Fuel Processing Technology 205 (2020) 106425. https://doi.org/https://doi.org/10.1016/j.fuproc.2020.106425.

[5] Y.B. Yang, A.N. Phan, C. Ryu, V. Sharifi, J. Swithenbank, Mathematical modelling of slow pyrolysis of segregated solid wastes in a packed-bed pyrolyser, Fuel 86(1-2) (2007) 169-180. https://doi.org/https://doi.org/10.1016/j.fuel.2006.07.012.

[6] Q. Xiong, Y. Yang, F. Xu, Y. Pan, J. Zhang, K. Hong, G. Lorenzini, S. Wang, Overview of computational fluid dynamics simulation of reactor-scale biomass pyrolysis, ACS Sustainable Chemistry & Engineering 5(4) (2017) 2783-2798. https://doi.org/https://doi.org/10.1021/acssuschemeng.6b02634.

[7] A.K. Olaleye, K.J. Adedayo, C. Wu, M.A. Nahil, M. Wang, P.T. Williams, Experimental study, dynamic modelling, validation and analysis of hydrogen production from biomass pyrolysis/gasification of biomass in a two-stage fixed bed reaction system, Fuel 137 (2014) 364-374. https://doi.org/https://doi.org/10.1016/j.fuel.2014.07.076.

[8] C. Ghabi, H. Benticha, M. Sassi, Two-dimensional computational modeling and simulation of wood particles pyrolysis in a fixed bed reactor, Combustion science and technology 180(5) (2008) 833-853. https://doi.org/https://doi.org/10.1080/00102200801894091.

[9] I. Malico, X. Zhou, J. Pereira, Two-dimensional numerical study of combustion and pollutants formation in porous burners, Combustion Science and Technology 152(1) (2000) 57-79. https://doi.org/https://doi.org/10.1080/00102200008952127.

[10] R.C.M. Filho, A.P. Pimenta, A two-dimensional numerical simulation of combustion and heat transfer in radiant porous burners, Combustion Science and Technology 183(4) (2011) 370-389. https://doi.org/https://doi.org/10.1080/00102202.2010.520278.

[11] L. Yermán, R.M. Hadden, J. Carrascal, I. Fabris, D. Cormier, J.L. Torero, J.I. Gerhard, M. Krajcovic, P. Pironi, Y.-L. Cheng, Smouldering combustion as a treatment technology for faeces: exploring the parameter space, Fuel 147 (2015) 108-116. https://doi.org/https://doi.org/10.1016/j.fuel.2015.01.055.

[12] T.L. Rashwan, J.I. Gerhard, G.P. Grant, Application of self-sustaining smouldering combustion for the destruction of wastewater biosolids, Waste management 50 (2016) 201-212. https://doi.org/https://doi.org/10.1016/j.wasman.2016.01.037.

[13] M.A.B. Zanoni, J. Wang, J.I. Gerhard, Understanding pressure changes in smouldering thermal porous media reactors, Chemical Engineering Journal 412 (2021) 128642. https://doi.org/https://doi.org/10.1016/j.cej.2021.128642.

[14] A.L. Duchesne, J.K. Brown, D.J. Patch, D. Major, K.P. Weber, J.I. Gerhard, Remediation of PFAS-Contaminated Soil and Granular Activated Carbon by Smoldering Combustion, Environmental Science & Technology 54(19) (2020) 12631-12640. https://doi.org/https://doi.org/10.1021/acs.est.0c03058.

[15] P. Pironi, C. Switzer, G. Rein, A. Fuentes, J.I. Gerhard, J.L. Torero, Small-scale forward smouldering experiments for remediation of coal tar in inert media, Proceedings of the Combustion Institute 32(2) (2009) 1957-1964. https://doi.org/http://dx.doi.org/10.1016/j.proci.2008.06.184.

[16] M.A. Zanoni, J.L. Torero, J.I. Gerhard, Determining the conditions that lead to self-sustained smouldering combustion by means of numerical modelling, Proceedings of the Combustion Institute 37(3) (2019) 4043-4051. https://doi.org/https://doi.org/10.1016/j.proci.2018.07.108.
[17] G. Sabadell, G. Scholes, D. Thomas, C. Murray, P. Bireta, G. Grant, D. Major, Ex situ treatment of organic wastes or oil-impacted soil using a smoldering process, Waste Management and the Environment IX 231(10) (2019) 367-376.
[18] G. Sabadell, D. Thomas, P. Bireta, G. Scholes, C. Murray, B. Boulay, G. Grant, D. Major, Treatment of oil-impacted soil and oily waste: overview of two field demonstration projects, SPE International Conference and Exhibition on Health, Safety, Security, Environment, and Social Responsibility, OnePetro, 2018.
[19] D. Thomas, P. Bireta, K. McVey, D. Segal, M. Hudson, B.-H. Sami, S. Gabriel, A Novel, Cost Effective and Easily Scaled Solution for On-Site Treatment of Oily Wastes, International Petroleum Technology Conference, OnePetro, 2020.
[20] R. Solinger, G.P. Grant, G.C. Scholes, C. Murray, J.I. Gerhard, STARx Hottpad for smoldering treatment of waste oil sludge: Proof of concept and sensitivity to key design parameters, Waste Management & Research (2020) 0734242X20904430. https://doi.org/https://doi.org/10.1177/0734242X20904430.
[21] J.I. Gerhard, G.P. Grant, J.L. Torero, Star: a uniquely sustainable in situ and ex situ remediation process, Sustainable Remediation of Contaminated Soil and Groundwater, Elsevier2020, pp. 221-246. https://doi.org/https://doi.org/10.1016/B978-0-12-817982-6.00009-4.
[22] M.A. Zanoni, J.L. Torero, J.I. Gerhard, Delineating and explaining the limits of self-sustained smouldering combustion, Combustion and Flame 201 (2019) 78-92. https://doi.org/https://doi.org/10.1016/j.combustflame.2018.12.004.
[23] V. Pozzobon, G. Baud, S. Salvador, G. Debenest, Darcy scale modeling of smoldering: impact of heat loss, Combustion Science and Technology 189(2) (2017) 340-365. https://doi.org/https://doi.org/10.1080/00102202.2016.1214585.
[24] H. Fadaei, M. Sennoune, S. Salvador, A. Lapene, G. Debenest, Modelling of non-consolidated oil shale semi-coke forward combustion: Influence of carbon and calcium carbonate contents, Fuel 95 (2012) 197-205. https://doi.org/https://doi.org/10.1016/j.fuel.2011.11.066.
[25] T.L. Rashwan, J.L. Torero, J.I. Gerhard, Heat losses in a smouldering system: The key role of non-uniform air flux, Combustion and Flame 227 (2021) 309-321. https://doi.org/https://doi.org/10.1016/j.combustflame.2020.12.050.
[26] M.F. Martins, S. Salvador, J.F. Thovert, G. Debenest, Co-current combustion of oil shale - Part 2: Structure of the combustion front, Fuel 89(1) (2010) 133-143. https://doi.org/https://doi.org/10.1016/j.fuel.2009.06.040.
[27] J. Yang, H. Chen, N. Liu, Modeling of two-dimensional natural downward smoldering of peat, Energy & Fuels 30(10) (2016) 8765-8775. https://doi.org/https://doi.org/10.1021/acs.energyfuels.6b02293.
[28] T.L. Rashwan, T. Fournie, J.L. Torero, G.P. Grant, J.I. Gerhard, Scaling up self-sustained smouldering of sewage sludge for waste-to-energy, Waste Management 135 (2021) 298-308. https://doi.org/https://doi.org/10.1016/j.wasman.2021.09.004.
[29] T.L. Rashwan, J.L. Torero, J.I. Gerhard, Heat losses in applied smouldering systems: Sensitivity analysis via analytical modelling, International Journal of Heat and Mass Transfer 172 (2021) 121150. https://doi.org/https://doi.org/10.1016/j.ijheatmasstransfer.2021.121150.
[30] T.L. Rashwan, J.L. Torero, J.I. Gerhard, The improved energy efficiency of applied smouldering systems with increasing scale, International Journal of Heat and Mass Transfer 177 (2021) 121548. https://doi.org/https://doi.org/10.1016/j.ijheatmasstransfer.2021.121548.
[31] S. Lin, X. Huang, Quenching of smoldering: Effect of wall cooling on extinction, Proceedings of the Combustion Institute 38(3) (2021) 5015-5022. https://doi.org/https://doi.org/10.1016/j.proci.2020.05.017.
[32] J.L. Torero, J.I. Gerhard, M.F. Martins, M.A. Zanoni, T.L. Rashwan, J.K. Brown, Processes defining smouldering combustion: Integrated review and synthesis, Progress in Energy and Combustion Science 81 (2020) 100869. https://doi.org/https://doi.org/10.1016/j.pecs.2020.100869.

[33] M.A. Zanoni, J.L. Torero, J.I. Gerhard, The role of local thermal non-equilibrium in modelling smouldering combustion of organic liquids, Proceedings of the Combustion Institute 37(3) (2019) 3109-3117. https://doi.org/https://doi.org/10.1016/j.proci.2018.05.177.
[34] G. Rein, A. Bar-Ilan, A.C. Fernandez-Pello, J.L. Ellzey, J.L. Torero, D.L. Urban, Modeling of one-dimensional smoldering of polyurethane in microgravity conditions, Proceedings of the Combustion Institute 30(2) (2005) 2327-2334. https://doi.org/https://doi.org/10.1016/j.proci.2004.08.150.
[35] G. Rein, A. Carlos Fernandez-Pello, D.L. Urban, Computational model of forward and opposed smoldering combustion in microgravity, Proceedings of the Combustion Institute 31(2) (2007) 2677-2684. https://doi.org/http://dx.doi.org/10.1016/j.proci.2006.08.047.
[36] G. Rein, C. Lautenberger, A.C. Fernandez-Pello, J.L. Torero, D.L. Urban, Application of genetic algorithms and thermogravimetry to determine the kinetics of polyurethane foam in smoldering combustion, Combustion and Flame 146(1-2) (2006) 95-108. https://doi.org/https://doi.org/10.1016/j.combustflame.2006.04.013.
[37] J. Yang, H. Chen, N. Liu, Heat Loss and Kinetic Effects on Extinction and Critical Self-Sustained Propagation of Forced Forward Smoldering, Fire Science and Technology 2015, Springer2017, pp. 831-840.
[38] N.A. Lutsenko, Numerical model of two-dimensional heterogeneous combustion in porous media under natural convection or forced filtration, Combust. Theor. Model. 22(2) (2018) 359-377. https://doi.org/https://doi.org/10.1080/13647830.2017.1406617.
[39] C. Di Blasi, Mechanisms of Two-Dimensional Smoldering Propagation Through Packed Fuel Beds, Combustion Science and Technology 106(1-3) (1995) 103-124. https://doi.org/10.1080/00102209508907769.
[40] A.B. Dodd, C. Lautenberger, A.C. Fernandez-Pello, Numerical examination of two-dimensional smolder structure in polyurethane foam, Proceedings of the Combustion Institute 32(2) (2009) 2497-2504. https://doi.org/http://dx.doi.org/10.1016/j.proci.2008.06.196.
[41] M. Moallemi, H. Zhang, S. Kumar, Numerical modeling of two-dimensional smoldering processes, Combustion and Flame 95(1-2) (1993) 170-182. https://doi.org/10.1016/0010-2180(93)90059-c.
[42] C. Ghabi, H. Benticha, M. Sassi, Parametric study of the heat transfer coefficient in bi-dimensional smoldering simulation, Thermal Science 11(4) (2007) 95-112. https://doi.org/https://doi.org/10.2298/TSCI0704095G.
[43] C. Ghabi, H. Benticha, M. Sassi, Computational modelling and simulation of forward-smouldering of porous media in a fixed bed, Progress in Computational Fluid Dynamics, an International Journal 7(5) (2007) 283-293. https://doi.org/https://10.1504/PCFD.2007.013889.
[44] A. Rostami, J. Murthy, M. Hajaligol, Modeling of a smoldering carbonaceous rod, Fuel Chemistry Division Preprints (2002).
[45] A. Rostami, J. Murthy, M. Hajaligol, Modeling of a smoldering cigarette, Journal of Analytical and Applied Pyrolysis 66(1-2) (2003) 281-301. https://doi.org/https://doi.org/10.1016/S0165-2370(02)00117-1.
[46] S.L. Macphee, J.I. Gerhard, G. Rein, A novel method for simulating smoldering propagation and its application to STAR (Self-sustaining Treatment for Active Remediation), Environmental modelling & software 31 (2012) 84-98. https://doi.org/https://doi.org/10.1016/j.envsoft.2011.11.004.
[47] T. Hasan, J.I. Gerhard, R. Hadden, G. Rein, Self-sustaining smouldering combustion of coal tar for the remediation of contaminated sand: Two-dimensional experiments and computational simulations, Fuel 150 (2015) 288-297. https://doi.org/https://doi.org/10.1016/j.fuel.2015.02.014.
[48] Y. Hu, Z. Wang, X. Cheng, C. Ma, Non-isothermal TGA study on the combustion reaction kinetics and mechanism of low-rank coal char, RSC advances 8(41) (2018) 22909-22916. https://doi.org/10.1039/C8RA02618A.
[49] B.A. Akash, W.S. O'Brien, The production of activated carbon from a bituminous coal, Int J Energy Res 20(10) (1996) 913-922. https://doi.org/10.1002/(SICI)1099-114X(199610)20:10<913::AID-ER205>3.0.CO;2-7.
[50] S. Arrhenius, Über die Reaktionsgeschwindigkeit bei der Inversion von Rohrzucker durch Säuren, Wilhelm Engelmann1889. https://doi.org/https://doi.org/10.1515/zpch-1889-0416.
[51] A.K. Galwey, M.E. Brown, Arrhenius parameters and compensation behaviour in solid-state decompositions, Thermochimica Acta 300(1-2) (1997) 107-115.
[52] A.K. Galwey, M.E. Brown, Application of the Arrhenius equation to solid state kinetics: can this be justified?, Thermochimica Acta 386(1) (2002) 91-98. https://doi.org/http://dx.doi.org/10.1016/S0040-6031(01)00769-9.

[53] A.K. Galwey, Thermal reactions involving solids: a personal view of selected features of decompositions, thermal analysis and heterogeneous catalysis, Journal of Thermal Analysis and Calorimetry 142(3) (2020) 1123-1144. https://doi.org/10.1007/s10973-020-09461-w.
[54] A.K. Galwey, E.B. Michael, A theoretical justification for the application of the Arrhenius equation to kinetics of solid state reactions (mainly ionic crystals), Proceedings of the Royal Society of London. Series A: Mathematical and Physical Sciences 450(1940) (1995) 501-512. https://doi.org/doi:10.1098/rspa.1995.0097.
[55] M.A.B. Zanoni, G. Rein, L. Yermán, J.I. Gerhard, Thermal and oxidative decomposition of bitumen at the Microscale: Kinetic inverse modelling, Fuel 264 (2020) 116704. https://doi.org/https://doi.org/10.1016/j.fuel.2019.116704.
[56] M.A. Zanoni, J.L. Torero, J.I. Gerhard, Determination of the interfacial heat transfer coefficient between forced air and sand at Reynold's numbers relevant to smouldering combustion, International Journal of Heat and Mass Transfer 114 (2017) 90-104. https://doi.org/https://doi.org/10.1016/j.ijheatmasstransfer.2017.06.020.
[57] S. Rosseland, Astrophysik: Auf atomtheoretischer grundlage, Springer-Verlag2013.
[58] U. Kleinhans, S. Halama, H. Spliethoff, The role of gasification reactions during pulverized solid fuel combustion: A detailed char combustion model based on measurements of char structure and kinetics for coal and pre-treated biomass, Combustion and Flame 184 (2017) 117-135. https://doi.org/https://doi.org/10.1016/j.combustflame.2017.05.033.
[59] R. Bogaard, P. Desai, H. Li, C. Ho, Thermophysical properties of stainless steels, Thermochimica Acta 218 (1993) 373-393. https://doi.org/https://doi.org/10.1016/0040-6031(93)80437-F.
[60] J.L. Torero, A.C. Fernandez-Pello, M. Kitano, Opposed Forced Flow Smoldering of Polyurethane Foam, Combustion Science and Technology 91(1-3) (1993) 95-117. https://doi.org/10.1080/00102209308907635.
[61] C.Y. Ho, T. Chu, Electrical resistivity and thermal conductivity of nine selected AISI stainless steels, Thermophysical and Electronic Properties Information Analysis Center …, 1977.
[62] D. Green, Perry R. Perry's Chemical Engineers' Handbook. 7 ediction, McGraw-hill New York, 1999.
[63] F.L. Yaggee, E. Gilbert, J. Styles, Thermal expansivities, thermal conductivities, and densities of vanadium, titanium, chromium and some vanadium-base alloys: A comparison with austenitic stainless steel, Journal of the Less Common Metals 19(1) (1969) 39-51. https://doi.org/https://doi.org/10.1016/0022-5088(69)90083-6.
[64] L. Kinsman, J. Torero, J. Gerhard, Organic liquid mobility induced by smoldering remediation, Journal of hazardous materials 325 (2017) 101-112. https://doi.org/https://doi.org/10.1016/j.jhazmat.2016.11.049.
[65] J. Wang, G.P. Grant, J.I. Gerhard, The influence of porous media heterogeneity on smouldering remediation, Journal of Contaminant Hydrology 237 (2021) 103756. https://doi.org/https://doi.org/10.1016/j.jconhyd.2020.103756.
[66] C. Switzer, P. Pironi, J.I. Gerhard, G. Rein, J.L. Torero, Self-Sustaining Smoldering Combustion: A Novel Remediation Process for Non-Aqueous-Phase Liquids in Porous Media, Environmental Science & Technology 43(15) (2009) 5871-5877. https://doi.org/10.1021/es803483s.
[67] F.P. Incropera, D.P. DeWitt, Fundamentals of heat and mass transfer, 3rd ed., Wiley, New York, 1990.
[68] G. Baud, S. Salvador, G. Debenest, J.-F. Thovert, New Granular Model Medium To Investigate Smoldering Fronts Propagation Experiments, Energy & Fuels 29(10) (2015) 6780-6792. https://doi.org/https://doi.org/10.1021/acs.energyfuels.5b01325.
[69] J. Porteiro, D. Patiño, J.L. Miguez, E. Granada, J. Moran, J. Collazo, Study of the reaction front thickness in a counter-current fixed-bed combustor of a pelletised biomass, Combustion and Flame 159(3) (2012) 1296-1302. https://doi.org/http://dx.doi.org/10.1016/j.combustflame.2011.10.007.
[70] M.A. Zanoni, J.L. Torero, J.I. Gerhard, Experimental and numerical investigation of weak, self-sustained conditions in engineered smouldering combustion, Combustion and Flame 222 (2020) 27-35. https://doi.org/https://doi.org/10.1016/j.combustflame.2020.08.020.